Approach for Monitoring Spatiotemporal Changes in Fractional Vegetation Cover Through Unmanned Aerial System-Guided-Satellite Survey: A Case Study in Mining Area

Shuang Wu ⓘ, Lei Deng ⓘ, Jun Zhai ⓘ, Zhuo Lu, Yanjie Wu, Yan Chen, Lijie Guo, and Haifeng Gao

Abstract—Fractional vegetation cover (FVC) is a vital indicator for monitoring regional vegetation and ecology. Although satellite remote sensing is used to monitor long-term changes in regional FVC, its applications are limited by the spatial resolution. Moreover, for unmanned aerial systems (UASs), obtaining long-term and large-scale images is difficult, and the efficiency of the synergy between UAS and satellite data for long-term FVC monitoring is limited. This article considered a mining area with extreme changes in vegetation as an example and proposed an efficient approach called multiple spatiotemporal-scale FVC prediction (MSFP) for long-term FVC monitoring in the region, which is based on the synergy of high spatial-resolution UAS data with high temporal-resolution Landsat data. First, we used the UAS imagery of several typical mining areas in Qianxi County of China collected in 2021, from which the vegetation information was extracted. Second, the 2-D Gaussian sampling was applied to aggregate, that is, to join/connect them into Landsat pixels. The vegetation index (VI) calculated from contemporary Landsat imagery was further used with the aggregated FVC of each satellite pixel. Finally, the VIs from the satellite imagery for different years were calibrated. The analysis demonstrated that: first, the proposed MSFP yielded improved the coefficient of determination (by 0.437) and decreased root-mean-square error (by 0.200) than the traditional dimidiate pixel method based on satellite imagery; second, the UAS imagery for few typical areas was used to predict the FVC of the large-scale area, thereby providing fine-scale vegetation information; third, the MSFP achieved high accuracy and long-term FVC monitoring by interyear calibration of VI calculated from Landsat data. This article paves the way toward accurate long-term monitoring of regional FVC. The demonstrated methodological framework is simple and operable, thereby opening the prospects for its applications in other environments.

Index Terms—Fractional vegetation cover (FVC), multiscale remote sensing, satellite imagery, unmanned aerial systems (UASs).

Shuang Wu, Lei Deng, Zhuo Lu, Yanjie Wu, and Lijie Guo are with the College of Resource Environment and Tourism, Capital Normal University, Beijing 100048, China (e-mail: 2200902139@cnu.edu.cn; denglei@cnu.edu.cn; 2200902185@cnu.edu.cn; 2210902132@cnu.edu.cn; 2190902147@cnu.edu.cn).

Jun Zhai, Yan Chen, and Haifeng Gao are with the Satellite Environment Application Center, Ministry of Ecology and Environment, Beijing 100094, China (e-mail: zhaij@lreis.ac.cn; chenyan30033@163.com; gaohf03@hotmail.com).

Digital Object Identifier 10.1109/JSTARS.2023.3284913

I. INTRODUCTION

VEGETATION is an essential component of terrestrial ecosystems, while vegetation growth is a key driver behind ecological changes [1]. Fractional vegetation cover (FVC) is a critical variable that characterizes vegetation by vertically projecting the areal proportion of a landscape occupied by green vegetation. Thus, FVC serves as an indicator of vegetation quality and ecosystem changes [2]. Mineral resource mining releases numerous pollutants into the environment, and resultant harmful substances can adversely affect vegetation growth. Vegetation in mining areas drastically changes over time. Therefore, accurately monitoring the long-term FVC changes is critical in large mining areas [3]. Traditional field measurement of FVC is time-consuming and labor-intensive, thereby hampering the large-scale monitoring of dynamic FVC changes. The development of remote sensing technology has recently paved the way toward fast and large-scale FVC monitoring in mining areas [4].

Despite its efficiency in retrieving FVC and its popularity in applications [5], [6], remote sensing has several issues. Fundamentally, some satellites (such as Landsat) were launched at early stages of the remote sensing technology development, which allowed them to accumulate sizable historical datasets with global scales and decadal span [7], [8]. Moreover, numerous methods for estimating FVC, such as empirical modeling and the mixed pixel decomposition model, have been developed. The most widely used methods include the dimidiate pixel model (DPM) [9] and the empirical model (EM) [10] between the measured FVC on the ground and the vegetation index (VI) calculated from satellite imagery. However, a common issue with mixed pixels in satellite imagery is that a single pixel will contain vegetation and other ground objects such as soil. Therefore, it will result in inaccurate vegetation information extraction, thereby reducing FVC prediction accuracy [11]. Furthermore, in DPM, obtaining the threshold value of VI in the calculation formula is difficult, causing uncertainty in the prediction of FVC. Considering the subjectivity of artificial ground measurements, the quadrat of field sampling of EM is typically 1–10^4 m^2, thereby indicating substantial differences in the pixel size of satellite imagery. There is a spatial mismatch between the survey plot size and the corresponding satellite pixel

size, which hinders the estimation of the FVC through an EM based on ground measurements and satellite data [12]. These factors prompt an urgent need for a method that can bridge this scale gap in the spatial dimension and improve FVC prediction accuracy.

In recent years, low-cost unmanned aerial systems (UASs), equipped with various microsensors, have quickly generated orthomosaic imagery using the structure from motion (SfM) algorithm. The UASs have been widely used in FVC monitoring [13], and previous studies have revealed that UASs combined with photogrammetry technology can provide imagery with centimeter-level spatial resolution, which can be used to improve the accuracy of FVC prediction [14]. UASs provide a quick, efficient, and clean method for acquiring ultrahigh spatial resolution data. Numerous approaches have been recently developed, including random forest (RF) regression, object-based image analysis, and spectral unmixing [15], [16]. Although these methods can provide ultrahigh spatial resolution FVC products, obtaining a wide range of images in the same area over many years using UAS itself is rather challenging. Even if multiphase UAS imagery is available, significant differences between the images can emerge owing to the impact of different environmental factors (cloudy or sunny, windy or windless) during each flight, thereby making long-term and large-scale FVC monitoring impossible [17].

Notably, satellite remote sensing can perform large-scale and long-term FVC monitoring; however, the satellite imagery has a coarse spatial resolution, thereby reducing the FVC prediction accuracy [18]. Therefore, although UAS remote sensing can provide high-accuracy vegetation monitoring, retrieving continuous images for many years is challenging [19]. Several recent studies have used UAS data to estimate FVC in synergy with coarser-resolution satellite images at global scales [20], [21], [22]. Moreover, the UAS imagery was upscaled to contemporary satellite pixels to obtain FVC for a certain period with a large scale and high accuracy. However, long-term FVC monitoring has not been achieved, thereby prompting the development of novel approaches that can effectively combine vegetation information from UAS and satellite imagery to achieve long-term, large-scale, high-accuracy FVC monitoring.

The main aim of this study was to develop an approach called multiple spatiotemporal-scale FVC prediction (MSFP) for monitoring spatiotemporal changes in FVC, which can effectively combine high spatial resolution UAS data and high temporal resolution Landsat data. Methodologically, our approach uses the classification results (vegetation and nonvegetation) of UAS imagery as ground measurement data. It was aggregated (i.e., joined or connected) into satellite pixels using 2-D Gaussian sampling, providing high-accuracy training samples for FVC estimation. Furthermore, the calibrated VI calculated from satellite images for many years was used in this method. Notably, the FVC estimation model could be applied to satellite images for many years through the interyear calibration of the VI calculated from satellite data.
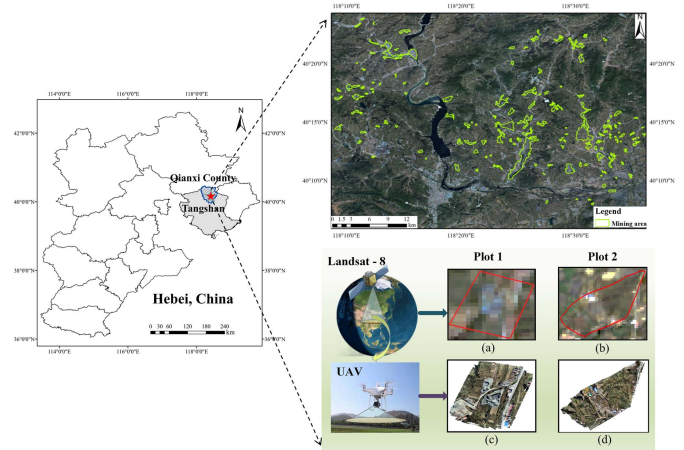

Fig. 1. Location of the study area. (a) and (b) Corresponding Landsat-8 imagery natural-color composite. (c) and (d) UAS orthomosaic imagery natural-color composite.
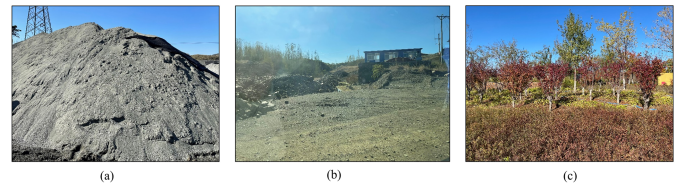

Fig. 2. Field survey photographs of mining area. (a) mined mining areas, (b) mining areas just after mining, (c) regreened mining areas.

II. Materials

A. Study Area

The study area, shown in Fig. 1, is the mining region of Qianxi County (39°57′15″–40°27′48″N, 118°6′49″–118°37′19″E), located in Hebei Province (China). The study area is characterized by a temperate continental monsoon climate, with an annual sunshine duration of 2303.1 h, annual average temperature of 11.7 °C, and annual average precipitation of 713.4 mm. Furthermore, the region has abundant mineral resources, with 470 million tons of iron ore reserves. The range of mining area is determined by the second national land survey of China, and its total area covers 3906.7 ha.

There are three typical mining areas in terms of vegetation coverage and ecological environment in field surveys: mined mining areas [almost no vegetation coverage, Fig. 2(a)], mining areas just after mining [little vegetation coverage, Fig. 2(b)], and regreened mining areas [more vegetation coverage, Fig. 2(c)].

B. UAS Data

The UAS data for three typical mining areas (low, medium, and high vegetation coverage) were collected between June 1 and June 3, 2021. A DJI Phantom 4 RTK quadcopter and its standard RGB camera were used, with 20 million effective pixels, the field of view of 84°, and the operating temperature of 0–40 °C. In this study, the flight altitude was set to 140 m, and the overlap of the side and heading were 70% and 80%, respectively.

TABLE I
IMAGERY SENSORS, ACQUISITION DATES, AND YEARS

Sensor	Year	Acquisition Date
L5 TM	2011	June 1
L8 OLI	2014	May 8
	2016	May 29
	2018	June 4
	2021	May 11

Pix4D mapper software (Pix4D SA, Lausanne, Switzerland) with the SfM algorithm generated a high-accuracy two-dimensional map with geographical coordinates from a single image captured by the UAS. Finally, we obtained 4 cm/pixel orthomosaic UAS imagery.

C. Landsat Data

Landsat 5 (L5) TM and Landsat 8 (L8) OLI images were downloaded from the Google Earth Engine. As the Landsat imagery should be as close as possible to the date of UAS flight (June 1 and June 3), the atmospherically corrected Landsat imagery (Level-2 Surface reflectance product) was obtained between early May and late June. When obtaining Landsat images from 2011 to 2021, only five Landsat images were used in the analysis (see Table I) owing to the impact of the sensor revisit period (16 days) and cloud cover per year.

The UAS and satellite data were coregistered to the Google imagery with the spatial resolution of 60 cm using the georeferencing tool from ArcGIS 10.2 software.

D. Reference Data

To validate the accuracy of estimated FVC using the proposed method, Google imagery with a spatial resolution of 60 cm was downloaded for 2011, 2014, 2016, 2018, and 2021. The acquisition date of Google imagery was ensured to be as close as possible to the date of the UAS flight.

III. METHODS

The workflow is summarized in Fig. 3. First, the vegetation information based on the UAS and satellite imagery was retrieved and used as the input parameters for the MSFP. Second, the vegetation information from the UAS imagery was aggregated into $30\,\text{m} \times 30\,\text{m}$ grids and subsequently aligned with the Landsat pixels to build the MSFP model by combining VI from Landsat imagery. Third, MSFP combined with UAS and Landsat imagery was applied to Landsat imagery in other years through the intercalibration of VI. Finally, the accuracy of the proposed MSFP was evaluated.
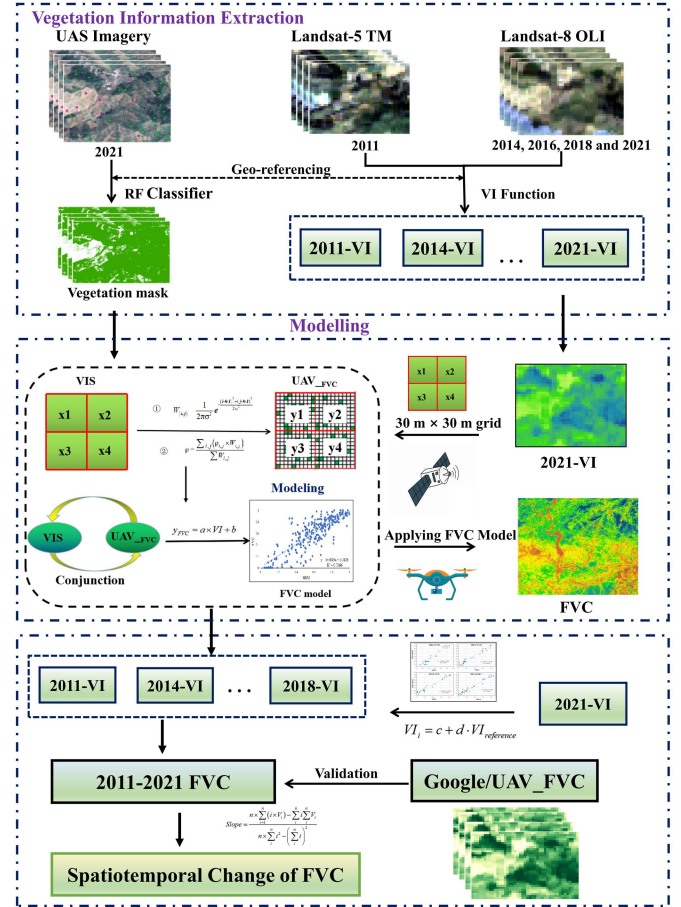

Fig. 3.   Workflow diagram of MSFP.

A. Vegetation Information Extraction

The extraction of vegetation information was divided into two parts. In the first part, we calculated four commonly used VIs based on satellite imagery. In the second part, we extracted high-resolution vegetation information based on the binary classification (vegetation and nonvegetation) of the UAS imagery.

In this study, we applied a series of VIs commonly used for vegetation monitoring, such as the simple ratio (SR), difference vegetation index (DVI), normalized difference vegetation index (NDVI), and enhanced vegetation index (EVI); all these VIs were calculated from Landsat imagery (see Table II). The SR was calculated using the near-infrared and red bands. Previous studies have indicated that SR is strongly positively correlated with physical and chemical vegetation parameters (such as the leaf area index, chlorophyll content, and FVC) and is widely used in FVC monitoring [21]. DVI was also selected because it reflects the health of vegetation growth [23]. In general, NDVI is one of the most used spectral indices in research. As NDVI is exceedingly sensitive to atmospheric effects and soil brightness, EVI can alleviate these shortcomings; its formula relies on the blue band to reduce the light scattering caused by air and soil brightness [24].

TABLE II
VI BASED ON SATELLITE IMAGERY

Index	Formulation	Reference
SR	SR=NIR/R	[25]
DVI	DVI=NIR–R	[26]
NDVI	NDVI=(NIR–R)/(NIR+R)	[27]
EVI	EVI=2.5[(NIR–R)/(NIR+6R–7.5B+1)]	[24]

Note: NIR, R, and B represent the near-infrared, red, and blue bands, respectively.

The RF classifier is a multi-decision-tree-integrated classifier [28]. The prediction ability of the classification model can be improved by using several different training sample subsets. In this way, we can increase the difference between the classification models. Compared to other machine learning algorithms, it stands out with stable performance, high accuracy, and few parameters required. It is widely used for remote-sensing image classification and vegetation change monitoring. Consequently, the RF classifier was utilized in this study to perform binary classification (0 = nonvegetation, 1 = vegetation) on UAS imagery. The performance of the RF classifier is determined by the number of decision trees and features [29]. The number of decision trees was set to 100, and the number of features was set to the square root of the number of input features [30]. The overall accuracy (OA) and kappa coefficient derived from the confusion matrix were both applied to evaluate the accuracy of the RF classification results [31]. The OA was estimated to be 97.1%, and the kappa coefficient was 0.966. The RF classification was carried out in ENVI 5.3 software, and the classification result assignment was carried out in ArcGIS 10.2 software.

B. Modeling

To make full use of the advantages of the high spatial resolution of UAVs and the high temporal resolution of satellite images, here is divided into the two parts. At the spatial scale, the vegetation information extracted from UAS imagery in 2021 was first aggregated to 30 m × 30 m grids by 2-D Gaussian sampling and subsequently aligned with the pixels of Landsat imagery in 2021. It was combined with the VI calculated from the Landsat imagery to build the FVC prediction model. At the time scale, the interyear VI calibration method was adopted to perform long-term FVC monitoring. The interyear calibration of VI is a conversion method applied to sensor data and was utilized to apply the FVC model to Landsat imagery for other years at the temporal scale.

The 2-D Gaussian sampling was used to aggregate the vegetation information extracted from the UAS imagery into 30 m × 30 m grids. Moreover, 2-D Gaussian sampling uses a weighted average, thereby implying a simple principle—the closer the grid cell, the greater the weight, and the farther the grid cell, the smaller the weight [28], [29]. The weights of each UAS pixel in the Landsat pixel were calculated. Each UAS pixel was assigned with a weight based on the 2-D Gaussian function, and 2-D Gaussian sampling was executed in MATLAB (The MathWorks, Release 2018b). The weight values were calculated based on the following:

$$W_{(i,j)} = \frac{1}{2\pi\sigma^2} e^{-\frac{(i-k-1)^2+(j-k-1)^2}{2\sigma^2}} \ (1 \leq i \leq 2k+1, 1 \leq j \leq 2k+1) \tag{1}$$

where $W_{(i,j)}$ represents the weight values of the pixels in rows i and columns j, and i and j are positive integers, which are the row and column numbers of each UAS pixel in a satellite pixel. The pixels in the upper-left corner are defined as (1,1). Thus, i gradually increases to the right and j gradually decreases. The window size defined by the 2-D Gaussian sampling is $(2k+1)$ $(2k+1)$. σ represents the standard deviation.

To obtain FVC corresponding to a Landsat grid after 2-D Gaussian sampling, the weight value of each UAS pixel was multiplied by the corresponding binary value obtained by RF classification. It was then divided by the sum of all UAS pixel weights in a Landsat grid. MATLAB (The MathWorks, Release 2018b) was applied to implement 2-D Gaussian sampling

$$\rho = \frac{\sum_{i,j} (\rho_{i,j} \times W_{i,j})}{\sum W_{i,j}} \tag{2}$$

where ρ is the FVC of a satellite pixel after aggregation, and $\rho_{i,j}$ is the value of the UAS pixels in rows i and columns j of a Landsat grid.

The unique ID number created by each Landsat pixel was used to join the VI calculated from the Landsat data and the aggregated FVC, thereby ultimately providing the training data. The FVC model was subsequently established by a linear regression. Linear regression is a statistical method widely used in the field of remote sensing for data analysis [30]. The specific formula is as follows:

$$y_{\text{FVC}} = a \times VI + b \tag{3}$$

where y_{FVC} represents the FVC value of Landsat pixels obtained by aggregation, and *VI* was calculated based on satellite imagery.

We applied the model established for Landsat images for the other years and ensured the consistency of Landsat imagery in the other years. Moreover, the calculated NDVI values from Landsat imagery were different to account for the variations in incident and reflected energy, atmospheric effects, sensor response, and band designations, which slightly vary between the Landsat sensors. In this study, the linear regression method proposed by Steven et al. [31] was utilized to calibrate the VI calculated from Landsat imagery in the other years with respect to the VI calculated from Landsat images in 2021. Notably, four VIs from Landsat imagery of 2021 used in this study were introduced into the model. The model was established based on vegetation information from Landsat and UAS imagery in 2021. The best VI was selected on this basis, and the interyear calibration of VI in other years was based on this VI in 2021.

The specific steps of the intercalibration of VI in different years were as follows.

1) Selecting an image as the reference image; VI calculated based on Landsat images in 2021 was selected as the reference image in this study.
2) Identifying some invariant targets spanning a range of VI values on the reference image and the calibrated image.
3) Calculating calibration coefficients between the reference image and the calibrated image.
4) Applying the calibration coefficients for each VI image from different years.

FVC over the years could then be predicted by substituting the calibrated VI over the years into (3), whereas the interannual calibration of VI was formalized by the following equation:

$$VI_i = c + d \cdot VI_{\text{reference}} \tag{4}$$

where VI_i is the VI value of the ith year; c and d are the intercept and slope, respectively; and $VI_{\text{reference}}$ is the VI value of imagery in the reference year; here, the reference year is 2021.

We calculated the slope of the FVC change curve from 2011 to 2021 to obtain the FVC change trend for each pixel in the image based on the following equation [32]:

$$Slope = \frac{n \times \sum_{i=1}^{n} (i \times V_i) - \sum_i^n i \sum_i^n V_i}{n \times \sum_i^n i^2 - \left(\sum_i^n i\right)^2} \tag{5}$$

where $Slope$ is the slope of the FVC change trend, n is the time series length, and V_i is the FVC in the ith year. If the slope > 0, the FVC of the mining area increases during the study period, indicating that the vegetation growth status has improved. If the slope < 0, the FVC of the mining area shows a downward trend during the study period, indicating that the vegetation growth status is deteriorating, and the higher the value, the faster the speed; otherwise, the change speed is slow [33].

According to previous studies and the actual conditions [34], [35], our results were classified into seven classes: severe degradation (class 1), moderate degradation (class 2), slight degradation (class 3), basically unchanged (class 4), slight improvement (class 5), moderate improvement (class 6), and significant improvement (class 7). Moreover, the raster calculator and reclassify tools in ArcMap v.10.2 were applied to quantify the slope of FVC.

C. Accuracy Evaluation

To evaluate the performance of the proposed MSFP, DPM, commonly used for long-term FVC monitoring based on satellite imagery, was used in this study. Fundamentally, DPM assumes that the NDVI value of each pixel comprises vegetation and soil and can be calculated using the following equation:

$$FVC_{DPM} = (NDVI - NDVI_{\text{soil}})/(NDVI_{\text{veg}} - NDVI_{\text{soil}}) \tag{6}$$

where FVC_{DPM} denotes the vegetation coverage, $NDVI_{\text{soil}}$ denotes the NDVI value of all the bare land pixels, and $NDVI_{\text{veg}}$ is the NDVI value of all vegetation pixels [36]. We selected an NDVI value with the cumulative frequency of 5% as $NDVI_{\text{soil}}$ and an NDVI value with a cumulative frequency of 95% as

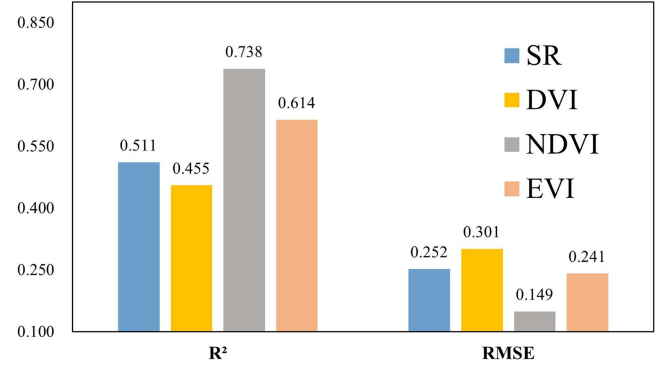Fig. 4.   Accuracy of models of UAS-derived FVC and SR, DVI, NDVI, and EVI derived from 2021 L8 imagery.

$NDVI_{\text{veg}}$ based on the actual studying conditions and previous studies.

Qualitative and quantitative analyses were performed to evaluate the accuracy of MSFP. We visually scrutinized the correspondence between the vegetation distribution and density of the reference image and the FVC estimated by the MSFP. To quantitatively evaluate the MSFP method, we randomly selected 70% of the data as training samples and 30% as test samples. The aggregated FVCs of Google imagery in 2011–2021 and 2021 UAV images were used as validation samples, and the aggregation was performed as detailed in the previous section. We subsequently calculated the coefficient of determination (R^2) and root-mean-square error (RMSE) to evaluate the performance of the method using (7) and (8) [37]

$$R^2 = 1 - \frac{\sum_{i=1}^{n} (y_i - \widehat{y_i})^2}{\sum_{i=1}^{n} (y_i - \overline{y})^2} \tag{7}$$

$$\text{RMSE} = \sqrt{\frac{\sum_{i=1}^{n} (y_i - \widehat{y_i})^2}{n}} \tag{8}$$

where y_i and $\hat{y}_i$ are the measured and predicted FVC values, respectively; $\overline{y}$ is the mean of the measured FVC; and n is the total number of samples in the testing set. The establishment of the FVC model and accuracy evaluation were both executed in MATLAB (The MathWorks, Release 2018b).

IV. RESULTS

A. Comparison Between MSFP and DPM

The four VIs calculated from Landsat imagery and 70% FVC aggregated from UAS images in 2021 were used as input in MSFP. And then, 30% FVC aggregated from UAS images 2021 evaluated the accuracy (see Fig. 4).

To select the best VI to construct the MSFP model, the accuracy of the four VIs was compared (see Fig. 4). Of the four VIs, DVI performed the worst ($R^2 = 0.455$, RMSE = 0.301), whereas EVI and SR performed well, with R^2 of 0.614 and 0.511 and RMSE of 0.241 and 0.252, respectively. NDVI performed the best and demonstrated the highest accuracy ($R^2 = 0.738$ and RMSE = 0.149). Thus, the NDVI-FVC model was used to build MSFP.

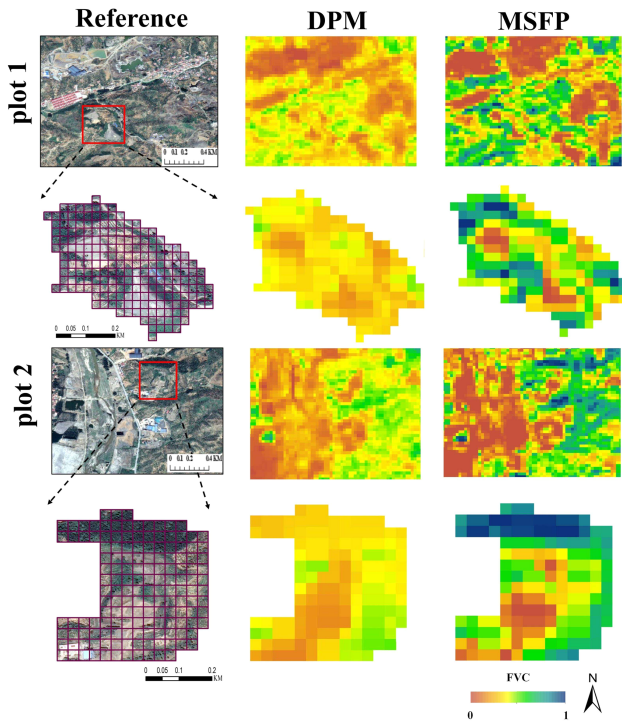Fig. 5. Results of accuracy validation based on two validation quadrats for MSFP and DPM in 2018.
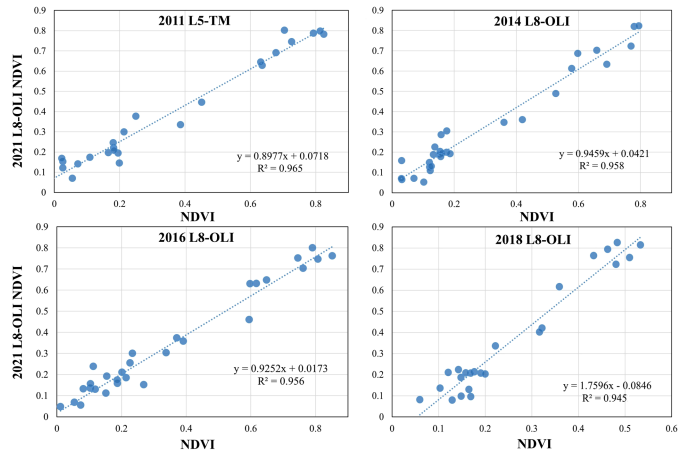

Fig. 6. Intercalibration of the NDVI calculated from Landsat images in 2011, 2014, 2016, and 2018. L8 image from 2021 was taken as the reference image and to calibrate the images from the other years.
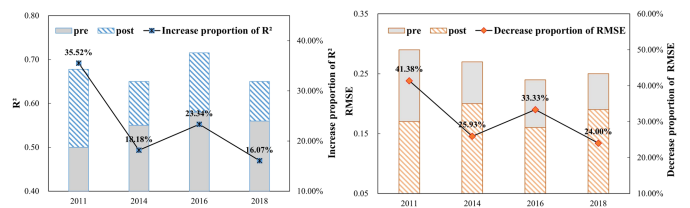

Fig. 7. Results of accuracy indicators for precalibration and postcalibration.

The MSFP and DPM estimated FVC in 2018 and were compared with the Google imagery after a 30 m× 30 m grid overlay. Two typical mining areas were selected, and local enlargement was demonstrated for the mine and its surrounding areas. The results are shown in Fig. 5. The FVC estimated by the MSFP was consistent with the specific distribution of vegetation and the density of vegetation coverage in the reference image. However, DPM underestimated FVC and misinterpreted the vegetation coverage area as a nonvegetation coverage area. Compared to the traditional DPM, the MSFP revealed more details, particularly in the intersection of nonvegetation and vegetation areas, such as roads and buildings. These findings suggest that MSFP performs better and presents more detailed information than DPM.

FVC calculated by MSFP and the widely used DPM were further statistically compared to the FVC calculated from the Google imagery in 2018. We found that MSFP achieved higher accuracy ($R^2 = 0.738$ and RMSE $= 0.149$), whereas traditional DPM had poor accuracy ($R^2 = 0.301$ and RMSE $= 0.349$). Moreover, prediction accuracy was higher for MSFP than for traditional DPM (R^2 increased by 0.437 and RMSE decreased by 0.2). These findings suggest that MSFP could combine the vegetation information of the UAS and Landsat imagery, thereby improving the accuracy of FVC estimation.

B. Effect of Interyear Calibration

To apply the model, established to the Landsat images for the other years, NDVI in 2021 was used to calibrate the NDVI for the other years (see Fig. 6).

NDVI calculated from the L5-TM imagery for 2011 was strongly positively correlated with NDVI in 2021 ($R^2 = 0.965$),

and high correlation was observed for NDVI calculated by the L8-OLI images in different years (2014, 2016, and 2018) ($R^2 > 0.94$). In summary, all NDVI values calculated from Landsat images in the other years (2011, 2014, 2016, and 2018) were strongly positively correlated with NDVI in 2021 ($R^2 > 0.94$), as shown in Fig. 6. The accuracy of the NDVI-FVC model combining the vegetation information of UAS and Landsat imagery in 2021, applied to the NDVI in the other years before (pre) and after the calibration (post), is shown in Fig. 7.

The accuracy of NDVI after calibration was higher than that of NDVI before calibration; R^2 increased by 23% on average, and RMSE decreased by 30% on average (see Fig. 7). In particular, NDVI after calibration was 35.52% higher than that before calibration, and the RMSE was 41.38% lower in 2011. This indicates that NDVI after the calibration can improve the accuracy of the FVC prediction.

To compare the effect of the NDVI before and after the calibration, NDVI values before and after calibration were introduced into the NDVI-FVC model, derived from UAS and Landsat imagery in 2021. Furthermore, the estimated FVC was visually compared with the distribution and intensity of the vegetation in the reference imagery, as shown in Fig. 8.

FVC was estimated using the NDVI before and after calibration in 2011 as an example. The FVC estimated by the NDVI after calibration was consistent with the specific distribution of vegetation and the area of vegetation coverage in the reference image (see Fig. 8). However, the FVC estimated by the NDVI before calibration was relatively consistent with the distribution
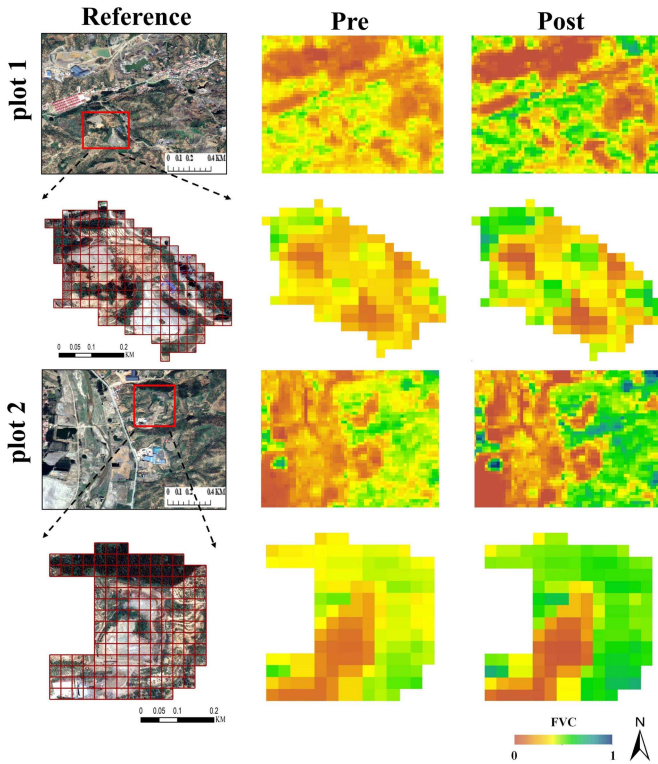
Fig. 8. Results of accuracy validation based on two validation quadrats for precalibration and postcalibration.

of vegetation. Compared with the accuracy of estimated FVC derived from the NDVI after calibration, the NDVI before calibration has lower accuracy of FVC prediction. For example, some areas with high vegetation coverage were misclassified as areas with low vegetation coverage. Overall, these results indicate that NDVI after calibration can improve the accuracy of FVC prediction, thereby achieving the best performance.

C. Spatiotemporal Changes in FVC

The FVC estimates for 2011, 2014, 2016, and 2018 were obtained after applying NDVI after calibration to the NDVI-FVC model for 2021 (see Fig. 9).

Overall, the mining area exhibited low FVC in 2011; however, the low vegetation coverage area was primarily clustered in the west of the mining area. Notably, the places with low FVC in the central and eastern regions were primarily rivers and slag accumulation areas in 2011 (see Fig. 9). The vegetation cover status improved in 2014, particularly in the eastern and western regions. While the vegetation coverage in 2016 and 2018 was the same, it became higher in 2014. The most abundant vegetation coverage was registered in 2021, thereby marking significant improvement than that in 2011, 2014, 2016, and 2018. The vegetation coverage gradually increased from 2011 to 2021, and the areas with low vegetation coverage were mostly rivers and slag accumulation areas. To dynamically monitor the changes in FVC, we calculated the slope change of the FVC curve from 2011 to 2021 (see Fig. 10).
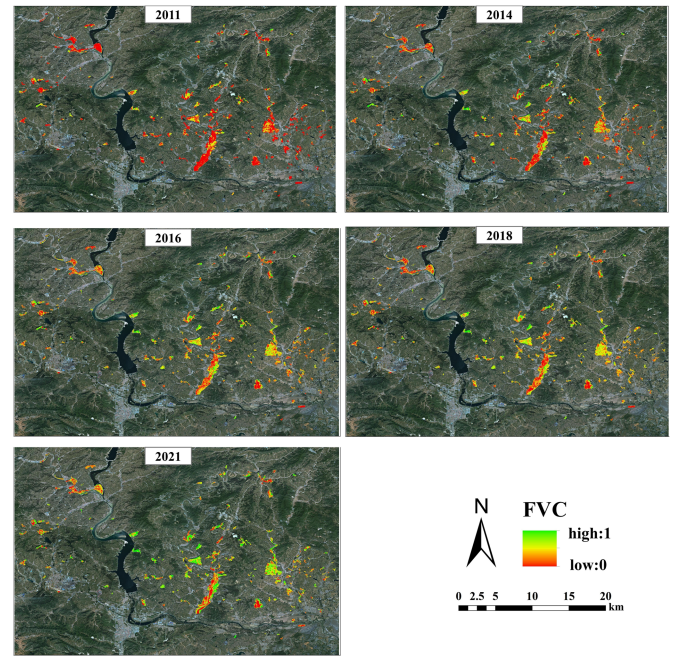

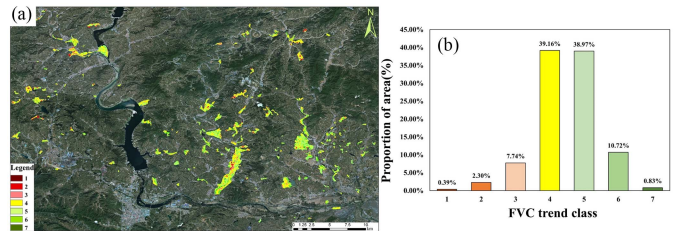Fig. 9. Changes in FVC in the mining area from 2011 to 2021.

Fig. 10. (a) Slope of the linear regression change trend in FVC from 2011 to 2021. (b) Area proportion of each class.

The spatial distribution of FVC changed from 2011 to 2020 (see Fig. 10). The degraded areas (class = 1, 2, and 3) were clustered in the west and middle of the mining area, while most of the mining areas were slightly or moderately improved. The statistics of each class demonstrated that the unchanged area and the area of slight improvement (classes 4 and 5) accounted for the most, with 39.16% and 38.97% of the area, respectively. The areas of slight degradation and moderate improvement (classes 3 and 6) accounted for 7.74% and 10.73%, respectively. The proportion of severe/moderate degradation (class = 1 or 2) and significant improvement (class = 7) was somewhat small, with less than 3%. Over the past decade, the FVC has been annually increasing, along with the gradual improvement of the ecological environment.

V. DISCUSSION

A. Influence of High-Resolution UAS Imagery

This study used a combination of UAS and satellite remote sensing to predict FVC by taking advantage from the ultrahigh spatial resolution of UAS imagery. In this way, we provided accurate training samples for the satellite image modeling, which

were consistent with previous studies [38]. Previous studies have revealed that manual collection of ground reference data is subjective, owing to the scale difference between ground-measured data and satellite images with coarse spatial resolution (such as Landsat) [39]. It is challenging to obtain ground-based observational references for spaceborne remote sensing data with coarse spatial resolution (such as Landsat). However, UAS stands out with two advantages for multiscale remote sensing applications than manual field measurements: 1) UAS data can achieve "surface to surface" aggregation, upscaling to the desired resolution. It can be matched with global-coverage satellite data, thereby allowing the estimation of physical and chemical parameters of vegetation or species classification in the global region. 2) UAS is a top-down observation with the same perspective as satellite remote sensing, which allows for avoiding the differences in observation results caused by different sensor perspectives.

Furthermore, the selection of samples is critical for estimating FVC. The sample value should encompass the whole FVC value interval, allowing for the selection of samples that are not overly centralized but distributed throughout each interval, therefore boosting the accuracy of FVC estimation. Our study used UAS imagery from several locations as the training samples. These areas ranged from low to high vegetation coverage, thereby providing favorable conditions for developing an FVC model. Our results were consistent with previous findings. In particular, Riihimäki et al. [21] collected UAS imagery from three typical Arctic areas (low, medium, and high vegetation coverage) and used satellite imagery to develop a model for FVC prediction. In the future, UAS imagery can be used instead of ground sampling to predict the physical and chemical parameters of plants (such as the leaf area index).

This study used FVC aggregated from 2021 UAV imagery as training and validation samples for the result of MSFP in 2021. For field survey, it has already been demonstrated that UAV-RGB imagery provides a rapid and reliable alternative for traditional field sampling with point frames [21], [40]. However, as the UAS imageries from 2011–2018 were not available, historical images were used as a supplement to verify the accuracy of the MSFP results. The Google images were classified into two categories (vegetation and nonvegetation), and the FVC was obtained by aggregating to a 30 m × 30 m grid to verify MSFP results. In this study, to investigate the validity of the FVC of Google image aggregation, the relative error between the FVC aggregated from Google imagery and FVC aggregated from UAS imagery was calculated. This difference was not significant (approximately 0.100), and their validation accuracy was similar ($R^2_{\text{Google}} = 0.708$, $\text{RMSE}_{\text{Google}} = 0.167$ and $R^2_{\text{UAV}} = 0.738$, $\text{RMSE}_{\text{UAV}} = 0.149$), indicating that the aggregated FVC of Google images can effectively validate MSFP results. Our method is consistent with that of previous studies, such as using Google images to validate the accuracy of feature classification [41], [42].

B. Multiscale-Data Aggregation

In this study, MSFP was estimated by combining vegetation information from the UAS and satellite imagery with the large-scale FVC from 2011 to 2021. The manual registration method was applied to align the UAS and satellite imagery, thereby implying that the UAS and satellite imagery were coregistered with Google imagery with a high spatial resolution. The results were consistent with previous research findings [30]. Furthermore, we found that the mutual matching problem of images with different spatial resolutions can be transformed into a machine learning optimization problem [43] by following some steps.

1) Create a moving window based on the size of the UAS image.
2) Move on the satellite image at a particular step length.
3) Calculate the matching degree between the two each time.
4) Take the image position at the best matching time as the final registration result.

Other georeferencing methods, such as direct and indirect georeferencing approaches [44], [45], have performed well as observed in previous studies and should be considered in future research.

The 2-D Gaussian sampling was used in this study, inconsistent with the methods used in previous studies. Most previous studies have used the simple average sampling method [21], [30], taking the average value of all pixels in the window as the value of the window. Despite some advantages, this approach has certain limitations. The simple average sampling method assigns the same weight to all pixels in the window. Thus, the pixel value at the edge of the window may exert a significant impact on the results. Although other sampling methods, such as nearest-neighbor sampling [46], have demonstrated some advantages for FVC monitoring applications, they have some limitations. This is because aggregation typically resamples remote sensing images by averaging or mathematically combining the values of the adjacent grid cells. These resamplings trigger an aggregation effect, thereby inevitably yielding less accurate statistical results. Furthermore, satellite-based approaches define the sampling area unit rather than the ecological or scientific scale [47]. In future research, we should consider additional applications of remote sensing data combined with the process of ecological evolution.

To elucidate the variations in the FVC estimation accuracy at different scales, we obtained the images with different spatial resolutions, for example, 4 m GaoFen-2 (GF-2), 10 m Sentinel-2, and 30 m Landsat-8, and built a multiscale FVC estimation model combined with 4 cm UAS imagery. The statistical analysis demonstrated that the 30 m Landsat imagery had the highest estimation accuracy ($R^2 = 0.738$ and $\text{RMSE} = 0.149$), whereas the accuracy of 10 m Sentinel-2 was comparable to that of 4 m GF-2, with R^2 of 0.54, and RMSE of 0.24. Although their statistical indicators were lower than those of 30 m Landsat-8, GF-2 and Sentinel-2 revealed more details in terms of visual effects (see Fig. 11) owing to their high spatial resolution. These results corresponded with those of previous studies [21], as several studies had previously found that upscaling to coarse-resolution remote sensing imagery, such as 30 m Landsat imagery, improves the accuracy of the estimated FVC. In contrast, when upscaling to finer spatial resolution remote sensing imagery, such as 4 m GF-2, the estimation accuracy of FVC is weakened [20], [21].
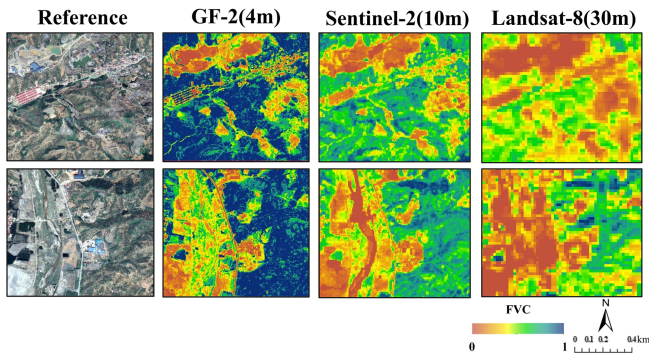
Fig. 11. Estimating FVC at multiple scales (GF-2, resolution = 4 m; Sentinel-2, resolution = 10 m; and Landsat-8, resolution = 30 m).

C. Temporal Calibration

In this study, the NDVI calculated from Landsat imagery was directly used for the temporal calibration. Previous studies have used relative radial calibration (or radial normalization; reference) to standardize the reflectance values [48]. Thus, the temporal dynamics of reflectance of each band of Landsat imagery can be calibrated. In this way, a more accurate VI of Landsat imagery can be obtained in temporal dimension, thereby paving the way toward multiscale and long-term FVC prediction. Previous studies have revealed that the changes in the position of the sun result in different solar radiation received at different surface locations, thereby causing some differences between remote sensing images obtained at different places, seasons, and periods [49]. Some studies [50], [51] have used the solar altitude angle calibration to perform temporal image calibration. The image obtained when the sun rays were vertically illuminated was calibrated to the image obtained when the sun rays were vertically illuminated. In this study, we calibrated the reflectivity and solar altitude angle of Landsat imagery from different years to determine the most appropriate calibration method.

Owing to the limitations of cloud conditions and the revisit period, we selected Landsat images for May–June in 2011, 2014, 2016, 2018, and 2021, where the spectral variation in vegetation was small and had less impact on interyear VI calibration in our study area. The selection of remote sensing images over a certain period in this study was similar to that of previous studies, such as those on long-time series vegetation monitoring in the vicinity of rivers [30], Australian dryland vegetation monitoring [52], and vegetation dynamics of coniferous and deciduous forests in Marmara Region, Turkey [53]. Furthermore, we evaluated the applicability of the MSFP in different time-phase images to improve the data acquisition convenience, facilitate the acquisition of the global data, and achieve the global FVC prediction. Overall, the potential of multiscale remote sensing to estimate FVC over multiple vegetation periods was elucidated. We obtained UAS and satellite data during the vegetation growth period (June) and during the vegetation nongrowth period (October). Consequently, we developed the MSFP with slightly higher estimation accuracy of the vegetation growth period ($R^2 = 0.738$ and RMSE = 0.149) than that of the nongrowth period model ($R^2 = 0.625$ and RMSE = 0.195). This indicates that although MSFP

can be used in various stages of vegetation, it can be deemed the most suitable for the growth period, which is consistent with previous research [54].

D. Uncertainty and Outlook

Owing to the uniqueness of the study area, NDVI outperformed EVI in terms of modeling performance of FVC. Almost no other green-covered features were identified in the study area other than vegetation. The vegetation canopy background of the mining area was primarily formed by bright bare rock and ore heaps. Thus, EVI, being highly sensitive to albedo, may not be ideally optimized to distinguish vegetation from sand using band differences. Furthermore, previous studies have reported a strong linear correlation between NDVI and FVC [55]. Thus, the greater the vegetation coverage, the lower the red-band reflectance and the higher the near-infrared band reflectance [56]. The red-band absorption quickly reached saturation, whereas the near-infrared band reflectance increased as the vegetation coverage increased. Moreover, previous studies have used vegetation indices for vegetation monitoring, including the green NDVI and infrared SR. In future research, additional VIs should be considered, and their differences to determine the VI suitable for all scales should be compared.

The mining area in Qianxi County (Hebei Province, China) was used as the study area in this work. The spatiotemporal changes in FVC in the mining area between 2011 and 2021 were determined using MSFP. MSFP offers evident theoretical and practical significance for restoring the ecological function of mining areas and for improving the quality of the ecological environment of the mining area. Our results revealed generally low vegetation coverage in 2011 owing to increased iron ore mining. However, the situation was significantly improved in 2014, likely owing to the implementation of tailored environmental protection measures and management systems by the Chinese government. Through these measures, all open-pit iron mines were either shut down or renovated since 2013 and were gradually turned to the ecological restoration of abandoned mines, such as planting trees in abandoned mining areas. Notably, we only examined the mining industry as an example for determining the potential of multiscale remote sensing technology for regional long-term FVC monitoring. Future studies should use multiscale remote sensing in other areas, such as typical ecological reserves.

VI. CONCLUSION

The regions that experience complex and intense changes in land cover, such as mining areas, require cost-effective mapping and monitoring using multiscale remote sensing technology. In this study, we proposed a novel methodology (MSFP) using UAS and satellite data for long-term monitoring of regional FVC. Our analysis demonstrated the following.

1) MSFP provided higher FVC prediction accuracy, with R^2 increased by 0.437 and RMSE decreased by 0.2, than the traditional DPM. Notably, the MSFP would reveal the visual features with more details than the traditional DPM based on satellite imagery.

2) Large-scale FVC will be obtained only by acquiring UAS imagery of several typical areas combined with contemporaneous satellite imagery.

3) By calibrating the VI calculated from Landsat imagery of other periods, the long-term and high-accuracy FVC can be easily obtained.

Our findings clearly showed that a synergy between multiscale remote sensing and UAS can significantly advance regional long-term FVC monitoring. We encourage broad use of UAS technologies in fieldwork, thereby advancing regional FVC monitoring in this way. Moreover, our results can aid in developing an automated system for FVC monitoring to provide data-driven guidelines beneficial for both researchers and policymakers focusing on vegetation dynamics.

ACKNOWLEDGMENT

REFERENCES

[1] D. Blok, G. Schaepman-Strub, H. Bartholomeus, M. M. P. D. Heijmans, T. C. Maximov, and F. Berendse, "The response of arctic vegetation to the summer climate: Relation between shrub cover, NDVI, surface albedo and temperature," *Environ. Res. Lett.*, vol. 6, no. 3, 2011, Art. no. 035502, doi: 10.1088/1748-9326/6/3/035502.

[2] M. J. Lara, I. Nitze, G. Grosse, P. Martin, and A. D. McGuire, "Reduced arctic tundra productivity linked with landform and climate change interactions," *Sci. Rep.*, vol. 8, no. 1, Feb. 2018, Art. no. 2345, doi: 10.1038/s41598-018-20692-8.

[3] W. Wang, R. Liu, F. Gan, P. Zhou, X. Zhang, and L. Ding, "Monitoring and evaluating restoration vegetation status in mine region using remote sensing data: Case study in Inner Mongolia, China," *Remote Sens.*, vol. 13, no. 7, 2021, Art. no. 1350, doi: 10.3390/rs13071350.

[4] P. R. Forsström, J. Juola, and M. Rautiainen, "Relationships between understory spectra and fractional cover in Northern European boreal forests," *Agricultural Forest Meteorol.*, vol. 308/309, 2021, Art. no. 108604, doi: 10.1016/j.agrformet.2021.108604.

[5] G. Yang et al., "Field monitoring of fractional vegetation cover based on UAV low-altitude remote sensing and machine learning," in *Proc. 10th Int. Conf. Agro-Geoinform.*, 2022, pp. 1–6.

[6] Y. Ghoussein et al., "Multitemporal remote sensing based on an FVC reference period using Sentinel-2 for monitoring Eichhornia crassipes on a Mediterranean river," *Remote Sens.*, vol. 11, no. 16, 2019, Art. no. 1856.

[7] X. Tong et al., "Quantifying the effectiveness of ecological restoration projects on long-term vegetation dynamics in the karst regions of Southwest China," *Int. J. Appl. Earth Observ. Geoinf.*, vol. 54, pp. 105–113, 2017, doi: 10.1016/j.jag.2016.09.013.

[8] F. H. Evans and J. Shen, "Long-term hindcasts of wheat yield in fields using remotely sensed phenology, climate data and machine learning," *Remote Sens.*, vol. 13, no. 13, 2021, Art. no. 2435, doi: 10.3390/rs13132435.

[9] K. Yan et al., "Evaluation of the vegetation-index-based dimidiate pixel model for fractional vegetation cover estimation," *IEEE Trans. Geosci. Remote Sens.*, vol. 60, Jan. 2022, Art. no. 4400514, doi: 10.1109/tgrs.2020.3048493.

[10] R. D. Graetz, R. P. Pech, and A. W. Davis, "The assessment and monitoring of sparsely vegetated rangelands using calibrated Landsat data," *Int. J. Remote Sens.*, vol. 9, no. 7, pp. 1201–1222, 2007, doi: 10.1080/01431168808954929.

[11] W. Chen et al., "Improving fractional vegetation cover estimation with shadow effects using high dynamic range images," *IEEE J. Sel. Topics Appl. Earth Observ. Remote Sens.*, vol. 15, pp. 1701–1711, Feb. 2022, doi: 10.1109/jstars.2022.3148282.

[12] H. E. Epstein, M. K. Raynolds, D. A. Walker, U. S. Bhatt, C. J. Tucker, and J. E. Pinzon, "Dynamics of aboveground phytomass of the circumpolar Arctic tundra during the past three decades," *Environ. Res. Lett.*, vol. 7, no. 1, 2012, Art. no. 015506, doi: 10.1088/1748-9326/7/1/015506.

[13] J. Dandois, M. Olano, and E. Ellis, "Optimal altitude, overlap, and weather conditions for computer vision UAV estimates of forest structure," *Remote Sens.*, vol. 7, no. 10, pp. 13895–13920, 2015, doi: 10.3390/rs71013895.

[14] Y. Niu, W. Han, H. Zhang, L. Zhang, and H. Chen, "Estimating fractional vegetation cover of maize under water stress from UAV multispectral imagery using machine learning algorithms," *Comput. Electron. Agriculture*, vol. 189, 2021, Art. no. 106414, doi: 10.1016/j.compag.2021.106414.

[15] B. Melville, A. Fisher, and A. Lucieer, "Ultra-high spatial resolution fractional vegetation cover from unmanned aerial multispectral imagery," *Int. J. Appl. Earth Observation Geoinf.*, vol. 78, pp. 14–24, 2019.

[16] R. Dunford, K. Michel, M. Gagnage, H. Piégay, and M. L. Trémelo, "Potential and constraints of unmanned aerial vehicle technology for the characterization of Mediterranean riparian forest," *Int. J. Remote Sens.*, vol. 30, no. 19, pp. 4915–4935, 2009, doi: 10.1080/01431160903023025.

[17] N. Chebrolu, T. Labe, and C. Stachniss, "Robust long-term registration of UAV images of crop fields for precision agriculture," *IEEE Robot. Autom. Lett.*, vol. 3, no. 4, pp. 3097–3104, Oct. 2018.

[18] Z. Wang, D.-X. Song, and D. Zhong, "Time-series reconstruction of 30M fractional vegetation cover based on multi-source satellite data," in *Proc. IEEE Int. Geosci. Remote Sens. Symp.*, 2022, pp. 6122–6125.

[19] N. Wang, Y. Guo, X. Wei, M. Zhou, H. Wang, and Y. Bai, "UAV-based remote sensing using visible and multispectral indices for the estimation of vegetation cover in an oasis of a desert," *Ecol. Indicators*, vol. 141, 2022, Art. no. 109155.

[20] J. Chen, S. Yi, Y. Qin, and X. Wang, "Improving estimates of fractional vegetation cover based on UAV in alpine grassland on the Qinghai–Tibetan Plateau," *Int. J. Remote Sens.*, vol. 37, no. 8, pp. 1922–1936, 2016, doi: 10.1080/01431161.2016.1165884.

[21] H. Riihimäki, M. Luoto, and J. Heiskanen, "Estimating fractional cover of tundra vegetation at multiple scales using unmanned aerial systems and optical satellite data," *Remote Sens. Environ.*, vol. 224, pp. 119–132, 2019, doi: 10.1016/j.rse.2019.01.030.

[22] S. Zhang et al., "Integrated satellite, unmanned aerial vehicle (UAV) and ground inversion of the SPAD of winter wheat in the reviving stage," *Sensors (Basel)*, vol. 19, no. 7, Mar. 2019, Art. no. 1485, doi: 10.3390/s19071485.

[23] M. Gunathilaka, "Modelling the behavior of DVI and IPVI vegetation indices using multi-temporal remotely sensed data," *Int. J. Environ., Eng. Educ.*, vol. 3, no. 1, pp. 9–16, 2021.

[24] A. Huete, K. Didan, T. Miura, E. P. Rodriguez, X. Gao, and L. G. Ferreira, "Overview of the radiometric and biophysical performance of the MODIS vegetation indices," *Remote Sens. Environ.*, vol. 83, no. 1/2, pp. 195–213, 2002.

[25] G. S. Birth and G. R. McVey, "Measuring the color of growing turf with a reflectance spectrophotometer[1]," *Agronomy J.*, vol. 60, no. 6, pp. 640–643, 1968.

[26] Y. Inoue, E. Sakaiya, Y. Zhu, and W. Takahashi, "Diagnostic mapping of canopy nitrogen content in rice based on hyperspectral measurements," *Remote Sens. Environ.*, vol. 126, pp. 210–221, 2012, doi: 10.1016/j.rse.2012.08.026.

[27] J. Rouse, R. Haas, J. Schell, and D. Deering, "Monitoring vegetation systems in the great plains with ERTS," in *Proc. 3rd Earth Resour. Technol. Satell.-1 Symp.*, 1974, pp. 301–317.

[28] R. Anniballe and S. Bonafoni, "A stable Gaussian fitting procedure for the parameterization of remote sensed thermal images," *Algorithms*, vol. 8, no. 2, pp. 82–91, 2015, doi: 10.3390/a8020082.

[29] J.-C. Padró, F.-J. Muñoz, L. Ávila, L. Pesquer, and X. Pons, "Radiometric correction of Landsat-8 and Sentinel-2A scenes using drone imagery in synergy with field spectroradiometry," *Remote Sens.*, vol. 10, no. 11, 2018, Art. no. 1687, doi: 10.3390/rs10111687.

[30] B. E. Morgan, J. W. Chipman, D. T. Bolger, and J. T. Dietrich, "Spatiotemporal analysis of vegetation cover change in a large ephemeral river: Multi-sensor fusion of unmanned aerial vehicle (UAV) and Landsat imagery," *Remote Sens.*, vol. 13, no. 1, 2020, Art. no. 51, doi: 10.3390/rs13010051.

[31] M. D. Steven, T. J. Malthus, F. Baret, H. Xu, and M. J. Chopping, "Intercalibration of vegetation indices from different sensor systems," *Remote Sens. Environ.*, vol. 88, no. 4, pp. 412–422, 2003, doi: 10.1016/j.rse.2003.08.010.

[32] A. B. Anderson, G. Wang, S. Fang, G. Z. Gertner, B. Güneralp, and D. Jones, "Assessing and predicting changes in vegetation cover associated with military land use activities using field monitoring data at Fort Hood, Texas," *J. Terramechanics*, vol. 42, no. 3/4, pp. 207–229, 2005, doi: 10.1016/j.jterra.2004.10.006.

[33] E. Ivits, M. Cherlet, W. Mehl, and S. Sommer, "Estimating the ecological status and change of riparian zones in Andalusia assessed by multi-temporal AVHHR datasets," *Ecol. Indicators*, vol. 9, no. 3, pp. 422–431, 2009, doi: 10.1016/j.ecolind.2008.05.013.

[34] D. Stow et al., "Variability of the seasonally integrated normalized difference vegetation index across the north slope of Alaska in the 1990s," *Int. J. Remote Sens.*, vol. 24, no. 5, pp. 1111–1117, 2003.

[35] Z. Gu, X. Duan, Y. Shi, Y. Li, and X. Pan, "Spatiotemporal variation in vegetation coverage and its response to climatic factors in the Red River Basin, China," *Ecol. Indicators*, vol. 93, pp. 54–64, 2018.

[36] G. Kyle and D. H. Duncan, "Arresting the rate of land clearing: Change in woody native vegetation cover in a changing agricultural landscape," *Landscape Urban Plan.*, vol. 106, no. 2, pp. 165–173, 2012, doi: 10.1016/j.landurbplan.2012.03.004.

[37] S. Wu, L. Deng, L. Guo, and Y. Wu, "Wheat leaf area index prediction using data fusion based on high-resolution unmanned aerial vehicle imagery," *Plant Methods*, vol. 18, no. 1, May 2022, Art. no. 68, doi: 10.1186/s13007-022-00899-7.

[38] E. Alvarez-Vanhard, T. Houet, C. Mony, L. Lecoq, and T. Corpetti, "Can UAVs fill the gap between in situ surveys and satellites for habitat mapping?," *Remote Sens. Environ.*, vol. 243, 2020, Art. no. 111780, doi: 10.1016/j.rse.2020.111780.

[39] D. A. Walker et al., "Circumpolar arctic vegetation: A hierarchic review and roadmap toward an internationally consistent approach to survey, archive and classify tundra plot data," *Environ. Res. Lett.*, vol. 11, no. 5, 2016, Art. no. 055005, doi: 10.1088/1748-9326/11/5/055005.

[40] N. Liu and P. Treitz, "Modelling high arctic percent vegetation cover using field digital images and high resolution satellite data," *Int. J. Appl. Earth Observ. Geoinf.*, vol. 52, pp. 445–456, 2016.

[41] Q. Hu et al., "Exploring the use of Google Earth imagery and object-based methods in land use/cover mapping," *Remote Sens.*, vol. 5, no. 11, pp. 6026–6042, 2013.

[42] H. Tian et al., "Garlic and winter wheat identification based on active and passive satellite imagery and the Google Earth Engine in Northern China," *Remote Sens.*, vol. 12, no. 21, 2020, Art. no. 3539.

[43] T. Gränzig, F. E. Fassnacht, B. Kleinschmit, and M. Förster, "Mapping the fractional coverage of the invasive shrub Ulex europaeus with multi-temporal Sentinel-2 imagery utilizing UAV orthoimages and a new spatial optimization approach," *Int. J. Appl. Earth Observ. Geoinf.*, vol. 96, 2021, Art. no. 102281, doi: 10.1016/j.jag.2020.102281.

[44] F. Benassi et al., "Testing accuracy and repeatability of UAV blocks oriented with GNSS-supported aerial triangulation," *Remote Sens.*, vol. 9, no. 2, 2017, Art. no. 172, doi: 10.3390/rs9020172.

[45] L. Jurjević, M. Gašparović, A. S. Milas, and I. Balenović, "Impact of UAS image orientation on accuracy of forest inventory attributes," *Remote Sens.*, vol. 12, no. 3, 2020, Art. no. 404, doi: 10.3390/rs12030404.

[46] S. Bhatnagar, L. Gill, S. Regan, S. Waldren, and B. Ghosh, "A nested drone-satellite approach to monitoring the ecological conditions of wetlands," *ISPRS J. Photogramm. Remote Sens.*, vol. 174, pp. 151–165, 2021, doi: 10.1016/j.isprsjprs.2021.01.012.

[47] S. J. Dark and D. Bram, "The modifiable areal unit problem (MAUP) in physical geography," *Prog. Phys. Geography, Earth Environ.*, vol. 31, no. 5, pp. 471–479, 2016, doi: 10.1177/0309133307083294.

[48] S. Furby and N. Campbell, "Calibrating images from different dates to 'like-value' digital counts," *Remote Sens. Environ.*, vol. 77, no. 2, pp. 186–196, 2001.

[49] S. E. Franklin and P. T. Giles, "Radiometric processing of aerial and satellite remote-sensing imagery," *Comput. Geosci.*, vol. 21, no. 3, pp. 413–423, 1995.

[50] S. Kobayashi and K. Sanga-Ngoie, "The integrated radiometric correction of optical remote sensing imageries," *Int. J. Remote Sens.*, vol. 29, no. 20, pp. 5957–5985, 2008, doi: 10.1080/01431160701881889.

[51] P. Meyer, K. I. Itten, T. Kellenberger, S. Sandmeier, and R. Sandmeier, "Radiometric corrections of topographically induced effects on Landsat TM data in an alpine environment," *ISPRS J. Photogramm. Remote Sens.*, vol. 48, no. 4, pp. 17–28, 1993.

[52] A. Sutton, A. Fisher, and G. Metternicht, "Assessing the accuracy of Landsat vegetation fractional cover for monitoring Australian drylands," *Remote Sens.*, vol. 14, no. 24, 2022, Art. no. 6322.

[53] N. Mashhadi and U. Alganci, "Evaluating BFASTMonitor algorithm in monitoring deforestation dynamics in coniferous and deciduous forests with LANDSAT time series: A case study on Marmara region, Turkey," *ISPRS Int. J. Geo-Inf.*, vol. 11, no. 11, 2022, Art. no. 573.

[54] M. Trombetti, D. Riano, M. Rubio, Y. Cheng, and S. Ustin, "Multi-temporal vegetation canopy water content retrieval and interpretation using artificial neural networks for the continental USA☆," *Remote Sens. Environ.*, vol. 112, no. 1, pp. 203–215, 2008, doi: 10.1016/j.rse.2007.04.013.

[55] M. Chiesi et al., "Monitoring and analysis of crop irrigation dynamics in Central Italy through the use of MODIS NDVI data," *Eur. J. Remote Sens.*, vol. 55, no. 1, pp. 23–36, 2022.

[56] C. J. Tucker, "Red and photographic infrared linear combinations for monitoring vegetation," *Remote Sens. Environ.*, vol. 8, no. 2, pp. 127–150, 1979.

Shuang Wu received the bachelor's degree in geographic information science (GIS) from Shandong Jianzhu University, Jinan, China, in 2020. She is currently working toward the master's degree in geographic information science (GIS) with the Capital Normal University, Beijing, China.

Her research interests include UAV remote sensing and its application in ecological environment research.

Lei Deng received the B.S. degree in cartography from Wuhan University, Wuhan, China, in 1998, and the Ph.D. degree in geography from Beijing Normal University, Beijing, China, in 2009.

He is currently a Professor with the School of Resources, Environment and Tourism, Capital Normal University, Beijing, China. His research interests include UAV remote sensing, data fusion and artificial intelligence, remote sensing, and GIS applications.

Jun Zhai received the Ph.D. degree in natural resources science from the Institute of Geography Science and Natural Resource Research, Chinese Academy of Sciences, Beijing, China, in 2013.

He works in the Satellite Environment Application Center, Ministry of Ecology and Environment, Beijing 100094, China. His current research focuses on remote sensing of ecological environment.

Zhuo Lu received the bachelor's degree in geographic information science (GIS) from Xi'an University of Science and Technology, Xi'an, China, in 2019. He is currently working toward the master's degree in surveying and mapping engineering with the Capital Normal University, Beijing, China.

His research interests include UAV remote sensing, lidar, and its application in ecological research.

Yanjie Wu received the bachelor's degree in geographic information science (GIS) from Shandong Normal University, Jinan, China, in 2021. She is currently working toward the master's degree in geographic information science (GIS) with the Capital Normal University, Beijing, China.

Her research interests include UAV remote sensing, lidar, and its application in ecological research.

Lijie Guo received the B.S. degree in geomatics engineering from Shangqiu Normal University, Shangqiu, China, in 2019. She is currently working toward the successive postgraduate and doctoral programs of study in geographic information science (GIS) with the Capital Normal University, Beijing, China.

Her research interests include remote sensing image processing and application and UAV forestry remote sensing.

Yan Chen received the M.S. degree in geographical science from the College of Urban and Environmental, Peking University, Beijing, China, in 2019.

She is currently an Engineer with the Satellite Environmental Center, Ministry of Ecology and Environment, Beijing, China.

Haifeng Gao received the Ph.D. degree in environmental ecology from Beijing Normal University, Beijing, China, in 2013.

He currently works in the Satellite Environment Application Center, Ministry of Ecology and Environment, Beijing 100094, China. His research interests include satellite remote sensing and its application in ecological research.